第 44 卷 第 9 期/2024 年 5 月/光学学报 研究论文

光学学报

共路移相干涉单像素波前成像用于透镜相位检测

陶星伏[1]，翟爱平[1*]，冀文静[1]，赵文静[1]，王东[1,2**]

[1]太原理工大学电子信息与光学工程学院，山西 太原 030024；

[2]太原理工大学新型传感器与智能控制教育部重点实验室，山西 太原 030024

摘要 传统的透镜相位测量技术很大程度上依赖于二维面阵探测器，其应用范围受限于面阵探测器的性能。单像素波前成像为此提供了一种新途径。本文提出将共路移相干涉单像素波前成像方法用于实际光学透镜的相位测量。以Hadamard基调制目标透镜波前，采用棋盘格参考方式，将空间传输光场分为信号光场和参考光场，构建共路移相干涉，单像素探测器采集相应的光强，由二阶相关方法重建被测透镜的波前信息，进而检测透镜相位。实验结果表明，对于名义焦距为1000 mm的透镜，以128 pixel×128 pixel重建相位图，拟合得到的透镜焦距的平均相对误差仅为0.0298%。该方法具有装置简单、成本低、计算量小等优点。此外，得益于单像素探测器自身优势，有望用于弱光环境，以及极紫外和远红外等特殊波段的透镜或透明物体的波前检测。

关键词 单像素波前成像；透镜相位检测；移相干涉；共路干涉

中图分类号 O439 **文献标志码** A **DOI**: 10.3788/AOS231982

1 引 言

从人们日常佩戴的眼镜到大型天文望远镜，所有光学仪器的设计过程中，透镜的相位信息至关重要[1-3]，但其无法被直接测量。现有间接测量透镜相位或波前的典型方法分别是基于干涉测量的波前传感[4-8]和基于角度测量的波前传感[9-10]。尽管它们在透镜波前测量方面取得了较大进展，但其探测性能通常依赖于光谱响应范围有限的二维探测器，例如电荷耦合器件（CCD）或互补金属氧化物半导体（CMOS）。然而，在深紫外、远红外、太赫兹等特殊波段二维探测器价格昂贵，或少数波段其尚不成熟甚至还没有的场合，传统基于二维探测器的方法应用受到限制。

基于单点探测器的单像素成像（SPI）技术[11-17]为此提供了一种新途径。单像素探测器具有弱光探测能力强、光谱响应范围广、制造成本低等优势，在散射成像[18]、多光谱成像[19-20]、X射线和太赫兹成像[21-24]、三维成像[25-27]等场合均展现出较大的潜力。

单像素成像过程中，被特定图案调制的探测光束与目标物体波前相互作用后被单像素探测器收集，再由二阶相关、压缩感知[28]或深度学习等重建目标信息。最近，研究人员在单像素波前成像方面进行了深入研究，并取得一定进展。Clemente等[29-31]提出利用双光路干涉仪即马赫-曾德尔干涉仪[29-30]或迈克尔孙干涉仪[31]辅助单像素探测器进行波前成像。然而，参考光束易受外界干扰，导致成像系统稳定性差、环境敏感，甚至产生额外的相位畸变。为了解决这一问题，国内外研究人员分别提出了不同参考方式、不同调制基与不同探测方式的单像素共路干涉波前成像方法[32-38]，并初步探讨了其在生物成像[34,38-39]等方面的应用。

本文提出将课题组自行搭建的共路干涉单像素波前成像系统应用于实际光学透镜的相位检测。基于高速数字微镜装置（DMD）以Hadamard基调制目标透镜波前，采用棋盘格参考方式，将空间传输光场分为信号光场和参考光场，构建共路移相干涉，单像素探测器记录相应的光强，由二阶相关方法重建被测透镜的波前相位。通过实验，研究了名义焦距分别为1000 mm和500 mm的光学透镜的相位检测；探究了不同空间分辨率和采样率对测量精度的影响；分析了单像素探测器前置针孔大小对测量精度的影响。本研究为光学透镜检测提供了新途径，同时也拓展了单像素波前成像技术的应用范围。

2 基本原理

2.1 实验原理

单像素成像利用编程可控的空间光调制器编码照

收稿日期：2023-12-25；**修回日期**：2024-02-21；**录用日期**：2024-02-22；**网络首发日期**：2024-03-13

基金项目：国家自然科学基金（62275188）、山西省国际科技合作项目（202104041101009）、山西省自然科学基金研究项目（202103021223091，20210302123169）

通信作者：*zhaiaiping@tyut.edu.cn；**wangdong@tyut.edu.cn

明结构光序列，利用单像素探测器采集每一帧照明结构光与被成像目标相互作用后光场的强度信息。多种结构光基底图案可用于编码照明光场，例如傅里叶(Fourier)基、离散余弦变换(DCT)、小波变换、轨道角动量(OAM)光束以及哈达玛(Hadamard)矩阵。其中，Hadamard矩阵作为二值矩阵的一种，能够轻易地通过DMD进行投影。因此，本文将其作为调制基用于编码照明光束。

图1(a_1)为部分用于编码照明光场的Hadamard基底图案。m阶Hadamard矩阵须满足$\boldsymbol{H}_m\boldsymbol{H}_m^{\mathrm{T}}=m\boldsymbol{I}$，其中$\boldsymbol{H}_m^{\mathrm{T}}$是矩阵$\boldsymbol{H}_m$的转置矩阵，$\boldsymbol{I}$是单位矩阵，任意阶Hadamard矩阵可以通过低阶矩阵之间的Kronecker积计算得到，如下式所示：

$$\boldsymbol{H}_{m+1}=\begin{bmatrix}\boldsymbol{H}_m & \boldsymbol{H}_m\\ \boldsymbol{H}_m & -\boldsymbol{H}_m\end{bmatrix}。\tag{1}$$

为了实现共路单像素移相干涉，需要使用参考方式将未知场划分为信号部分和参考部分，常用的参考方式包括随机参考、外参考和棋盘格参考等[34]，考虑到成像时间、成像视场以及成像分辨率的需求，选择棋盘格参考用来演示本文所提出的方法。如图1(a)和1(b)所示，分别为信号光场和参考光场的编码过程。将Hadamard调制基[图1(a_1)]与棋盘格[图1(a_2)]编码得到信号光场[图1(a_3)]。为了控制参考光场和信号光场之间的相对相位，信号光场相位保持不变，而参考部分则需要对其进行移相。这里以四步移相为例，设置相移量$\Delta\varphi$的值分别为0、$\pi/2$、π、$3\pi/2$，如图1(b_2)所示，将周期为4个像素的二元光栅与反棋盘格[图1(b_1)]叠加用来对参考部分实现四步移相，得到如图1(b_3)所示编码后的参考光场。如图1(c)所示，信号光场与参考光场干涉后的一阶衍射光通过透镜被傅里叶变换后，经针孔滤波，其零频分量被单像素探测器探测。因此，干涉强度由下式给出：

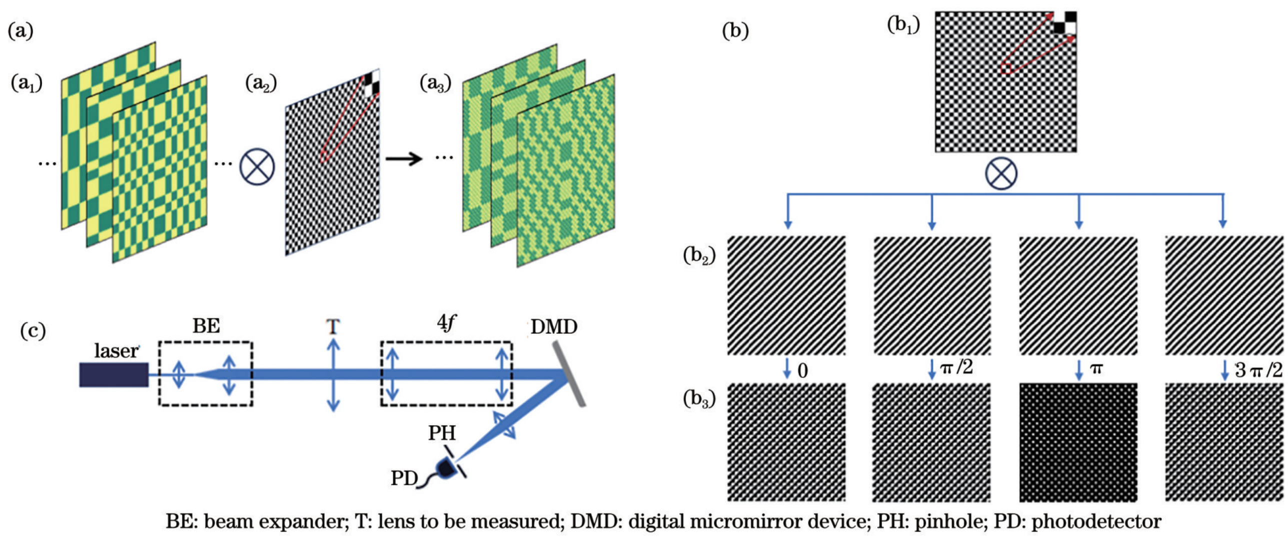

图1 调制图案构成和成像光路示意图。(a)、(b)信号光场和参考光场的编码过程示意图：(a_1) Hadamard图案；(a_2)棋盘格，用于引入信号光场；(a_3) DMD上用于引入信号光的图案；(b_1)反棋盘格，用于引入参考光场；(b_2)二元移相光栅，用于引入四步移相；(b_3) DMD上用于引入参考光的图案；(c)成像光路示意图

Fig. 1 Schematic diagrams of pattern construction and light path. (a), (b) Schematic diagrams of coding processes of signal light and reference light: (a_1) Hadamard pattern; (a_2) checkerboard for introducing signal light; (a_3) patterns on DMD for introducing signal light; (b_1) inverted version of checkerboard for introducing reference light; (b_2) binary phase-shifting gratings for introducing four-step phase shifts; (b_3) patterns on DMD for introducing reference light; (c) schematic diagram of light path

$$I_{\varphi_r+\Delta\varphi}=\left|\iint\left[S(x,y)+E(x,y)\right]\times \exp\left[-\mathrm{i}\cdot 2\pi\left(xf_x+yf_y\right)\right]\mathrm{d}x\mathrm{d}y\Big|_{f_x=f_y=0}\right|^2,\tag{2}$$

式中：(x,y)表示空间坐标；f_x和f_y分别为光场沿x轴和y轴的空间频率；$E(x,y)$表示参考光场的相干叠加；$S(x,y)$是第n阶Hadamard图案调制后的信号光场，分别可以表示为

$$E(x,y)=A_r(x,y)\cdot\exp\left\{\mathrm{i}\left[\varphi_r(x,y)+\Delta\varphi\right]\right\},\tag{3}$$

$$S(x,y)=P_n(x,y)O(x,y),\tag{4}$$

式中：$A_r(x,y)$表示反棋盘格与目标透镜的叠加；$\Phi_r(x,y)$表示参考光场与信号光场的初始相位差；$P_n(x,y)$表示棋盘格与第n阶Hadamard图案的叠加；$O(x,y)$表示图1(c)中待测透镜的波前。复系数Y_n可以由三步移相或者四步移相计算：

三步移相：

$$Y_n=\frac{1}{6}\left[\left(2I_{\varphi_r}-I_{\varphi_r+2\pi/3}\right)+\mathrm{i}\sqrt{3}\left(I_{\varphi_r+2\pi/3}-I_{\varphi_r+4\pi/3}\right)\right],\tag{5}$$

四步移相：

$$Y_n=\frac{1}{4}\left[\left(I_{\varphi_r}-I_{\varphi_r+\pi}\right)+\mathrm{i}\left(I_{\varphi_r+\pi/2}-I_{\varphi_r+3\pi/2}\right)\right]。\tag{6}$$

然后透镜波前 $O'(x,y)$可以通过二阶相关算法重构：

$$O'(x,y)=\frac{1}{K}\sum_{n=1}^{K}Y_n\cdot H_n(x,y),\tag{7}$$

式中：K为重建图像的像素总数；$H_n(x,y)$表示第 n 阶 Hadamard 图案。被测光学透镜的相位可以从重构的波前中计算：

$$\varphi_1(x,y)=\arg[O'(x,y)]。\tag{8}$$

2.2 实验结果

采用波长为 532 nm 的激光器作为光源，如图 2 所示，激光分别经过扩束器、被测透镜，以及 4f 成像系统（由焦距同为 50 mm 的透镜 L_0 和透镜 L_1 组成），将携带被测光学透镜波前信息的光场中继在 DMD（Vialux V-6501）平面上，而后被 DMD 预先加载的编码图案调制。DMD 的刷新频率为 10.3 kHz，总像素数为 1920 pixel×1080 pixel，像元尺寸为 7.6 μm。为了使单像素探测器最大程度地收集出射光的强度信息，在光路中放置焦距为 150 mm 的会聚透镜 L_2。信号光场与参考光场干涉后的一阶衍射光经透镜 L_2 傅里叶变换后，用针孔滤出一阶衍射光的零频分量，并用单像素探测器（KG-PR-200K-A-FS）收集其强度信息。然后，经数据采集卡（NI USB-6216）将光信号数字化。

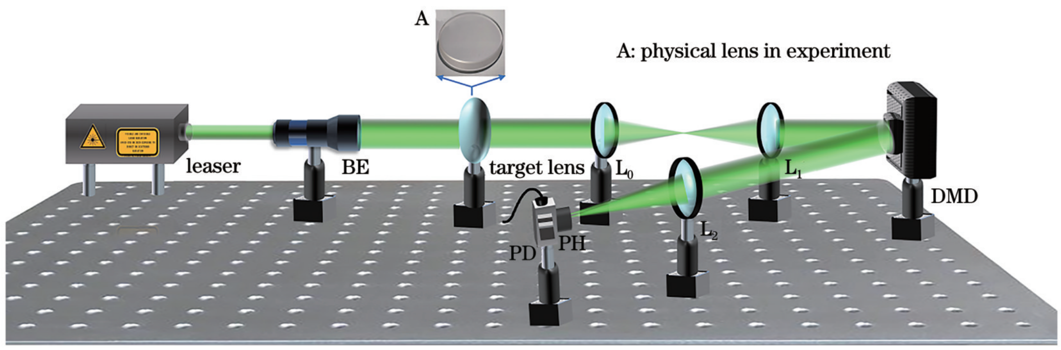

图 2　实验装置

Fig. 2　Experimental setup

实验中，分别选取名义焦距为 1000 mm（大恒光电，GCL-010626A）和 500 mm（大恒光电，GCL-010611A）的双胶合透镜作为被测目标。为了保证足够的成像信噪比，将 DMD 的 2×2 个微镜合并为一个成像像素，共 512×512 个微镜用来实现调制基图案的切换。为了实现棋盘格参考，至少需要将 2×2 个成像像素合并为一个超像素，即一个超像素由 4×4 个 DMD 微镜组成。最终，成像的空间分辨率为 128 pixel×128 pixel。图 3(a)和 3(d)分别显示了基于四步移相和二阶相关算法重建的两个名义焦距不同的透镜相位。

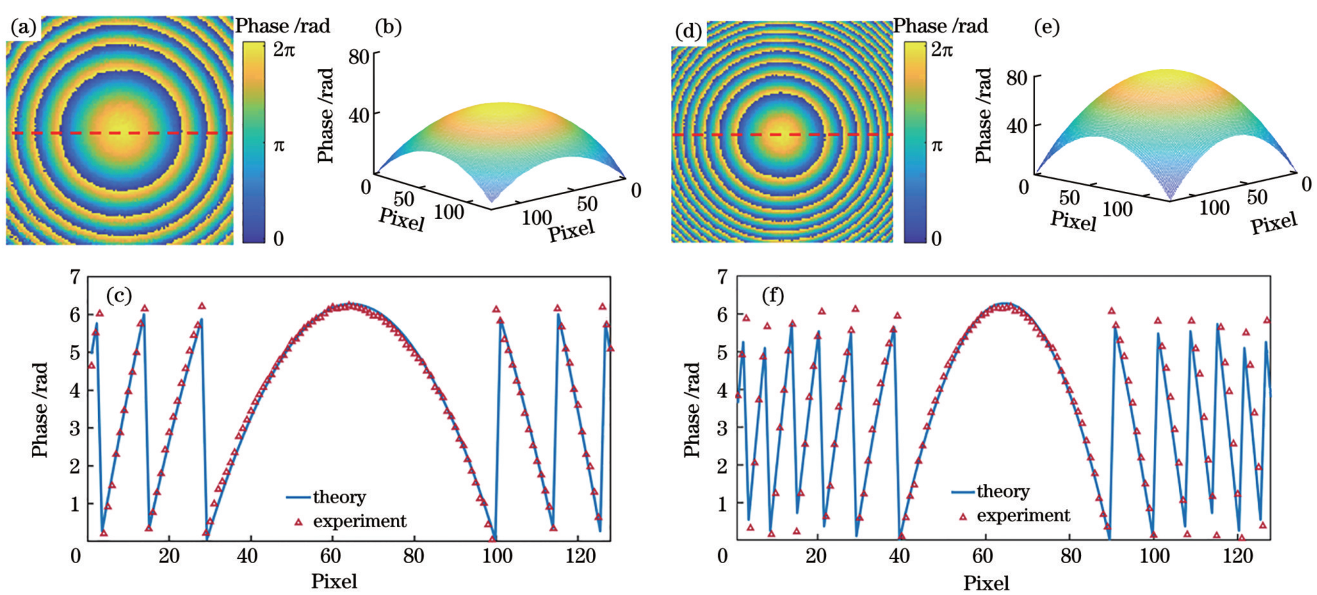

图 3　名义焦距为 1000 mm 和 500 mm 光学透镜的相位检测结果。(a)、(d)截断相位分布；(c)、(f)测量相位的横截面（三角形）与理论值（实线）的对比；(b)、(e)对应的去包裹相位的三维图

Fig. 3　Phase detection results of optical lenses with nominal focal lengths of 1000 mm and 500 mm. (a), (d) Truncating phase distribution; (c), (f) cross-sections of measured phases (triangles) compared with theoretical values (solid lines); (b), (e) 3D display of corresponding unwrapped phase

将图 3(a)和 3(d)中虚线上的相位检测值突出显示，如图 3(c)和 3(f)中的三角形所示，透镜相位的理论值如图 3(c)和 3(f)中实线所示，两者吻合效果很好。将图 3(a)和 3(d)中的截断相位展开得到透镜的连续相位曲面，如图 3(b)和 3(e)所示，根据透镜曲率和焦距的关系即可计算得到透镜的焦距。与名义焦距值为 1000 mm 和 500 mm 对应的实验焦距测量值分别为 1000.2 mm 和 499.5 mm，实验测量的相对误差分别为 0.02% 和 −0.10%。以上结果证明，基于 DMD 的单像素共路干涉(DSCI)成像方法对透镜相位的检测是有效的。此外，比较两个不同焦距透镜的实验测量值发现，当被测透镜焦距变小时，测量精度略有下降，这与传统方法所得结论一致。

该方法的误差来源可能包括环境噪声、光源波动、光路搭建以及针孔的滤波。为了验证不同的针孔尺寸对测量结果的影响，分别采用直径为 15 μm 和 25 μm 的针孔滤出一级衍射光的零频分量，对名义焦距为 1000 mm 的光学透镜进行相位检测，并将测量结果与上述实验结果对比，如表 1 所示。可见，针孔尺寸的选择对透镜的测量精度有不可忽略的影响，针孔尺寸越小，测量精度越高。然而，考虑到探测的信噪比，针孔尺寸不能无限缩小。采用折中的方案，以下实验仍选择直径为 20 μm 的针孔对光束进行滤波。

表 1 不同尺寸针孔滤波对名义焦距为 1000 mm 的光学透镜的测量结果

Table 1 Measurement results of optical lens with nominal focul length of 1000 mm filtering with different sizes of pinholes

Size of pinhole /μm	Measured value /mm	Relative error /%
15	999.944	−0.0056
20	1000.184	+0.0184
25	999.365	−0.0635

为了验证低分辨率下 DSCI 对透镜相位检测的有效性，以 64 pixel×64 pixel 为例，采用四步移相法对名义焦距为 1000 mm 的物理透镜进行相位检测。相应的截断相位及其截面如图 4 所示，由此计算得到的透镜焦距测量值为 1001.28 mm，相对误差为 0.128%。

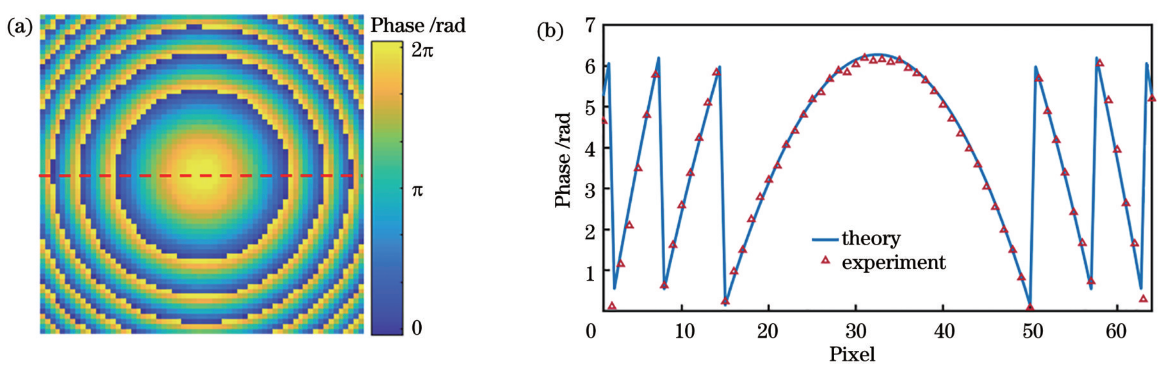

图 4 空间分辨率为 64 pixel×64 pixel 的光学透镜(名义焦距为 1000 mm)的相位检测结果。(a)截断相位轮廓；(b)测量相位的横截面(三角形)与理论值(实线)的对比

Fig. 4 Phase detection results of optical lenses (nominal focul length is 1000 mm) with resolution of 64 pixel×64 pixel. (a) Truncating phase contour; (b) cross-sections of measured phases (triangles) compared with theoretical values (solid lines)

基于不同空间分辨率的透镜相位图像，对名义焦距为 1000 mm 的光学透镜分别进行 5 次相位检测和焦距计算。表 2 和表 3 分别给出了基于 128 pixel×128 pixel 和 64 pixel×64 pixel 的透镜相位图像得到的焦距测量值和相对误差。焦距测量值的平均值分别为 1000.080 mm 和 999.422 mm，平均相对误差分别为 0.0298% 和 0.1603%，可见，透镜相位图像空间分辨率越高，焦距的测量值越接近理论值，进一步证明了 DSCI 用于实际光学透镜相位测量的可行性和稳定性。

表 2 128 pixel×128 pixel 透镜相位图像对应的焦距测量值与理论值的比较

Table 2 Comparison of measured focal lengths with theoretical values from lens phase map with resolution of 128 pixel×128 pixel

Measured value /mm	1000.184	1000.380	999.750	1000.379	999.705
Relative error /%	+0.0184	+0.0380	−0.0250	+0.0379	−0.0295

表 3 64 pixel×64 pixel 透镜相位图像对应的焦距测量值与理论值的比较

Table 3 Comparison of measured focal lengths with theoretical values from lens phase map with resolution of 64 pixel×64 pixel

Measured value /mm	998.144	998.330	1001.282	1001.280	998.073
Relative error /%	−0.1856	−0.1670	+0.1282	+0.1280	−0.1927

本文基于移相干涉方法求解信号场和参考场间的干涉项。对于四步移相法，对应Hadamard基的每一幅调制图案，参考光场都要经过四步移相才能得到透镜的截断相位。若采用三步移相法，总的测量时间将减少25%，可实现更高的测量效率。图5为基于三步移相法获得的透镜相位。由图5(b)和5(d)计算得到的透镜焦距测量值分别为1000.6 mm和501.6 mm。与理论值相比，相对误差分别为0.06%和0.32%。

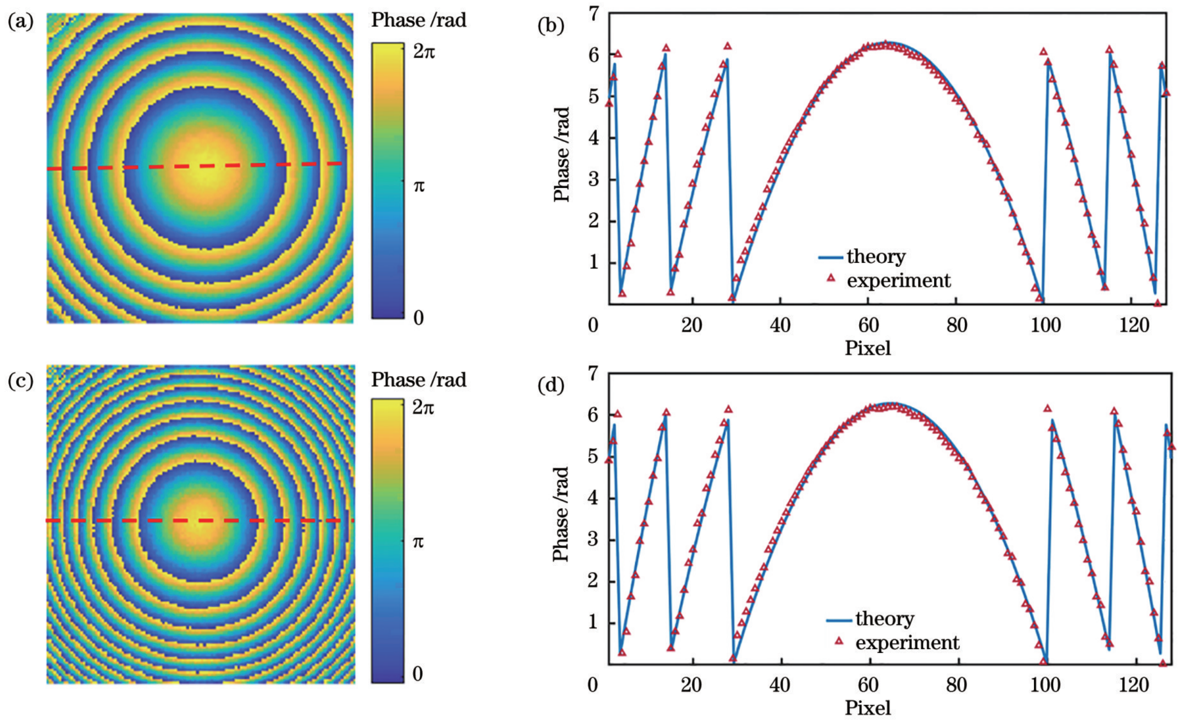

图5　采用三步移相法测量名义焦距为1000 mm和500 mm光学透镜的相位检测结果。(a)、(c)截断相位分布；(b)、(d)测量相位的横截面(三角形)与理论值(实线)的对比

Fig. 5　Phase detection results of optical lenses with nominal focal lengths of 1000 mm and 500 mm measured using three-step phase-shift method. (a), (c) Truncating phase distribution; (b), (d) cross-sections of measured phases (triangles) compared with theoretical values (solid lines)

除了减少移相次数，在单像素成像中，还可以通过降采样策略，即只采集少部分频谱系数来减少测量次数和成像时间。此处，采用三步移相法结合降采样策略重建透镜相位。图6给出采样率分别为0.8和0.4时，针对名义焦距为1000 mm的光学透镜重建的截断相位以及与理论值的对比曲线。计算可得，焦距测量值分别为1001.4 mm和1001.9 mm，相对误差分别为0.14%和0.19%。对于名义焦距为500 mm的光学透镜，如图7所示，采样率为0.8和0.4时，焦距的测量值分别为503.1 mm和503.4 mm，相对误差分别为0.62%和0.68%。

3　分析与讨论

本文提出一种基于DMD共路移相干涉单像素波前成像的光学透镜相位检测方法。对于名义焦距为1000 mm的光学透镜，采用四步移相干涉法对其相位进行重建，当重建相位空间分辨率为128 pixel×128 pixel时，计算得到焦距的测量值的平均相对误差低至0.0298%。同时，为了缩短透镜相位检测时间，在DMD内存一定的情况下，采用三步移相干涉法和降采样策略检测光学透镜的相位。实验结果表明，与四步移相干涉法相比，精度虽有所下降，但仍然可以通过检测的透镜相位计算得到相对精确的焦距测量值。

得益于单像素探测器的低成本优势，本文所提方法提供了一种可见光波段的高性价比透镜相位检测方案。其次，单像素探测器的宽光谱、高灵敏响应能力[19-20]，使得该方法有望用于深紫外、远红外、太赫兹等特殊波段，以及二维探测器价格昂贵，或少数波段二维探测器尚不成熟甚至还没有的场合。同时，它还可以在重建的相位图像中直接观察光学透镜是否存在制造上的瑕疵，或者基于相位的三维轮廓判断透镜是否存在像散、彗差等。此外，如果采用宽场照明，该方法还有望用于光学透镜的色差标定。在缩短检测或者成像时间方面，可以采用基于深度Q学习网络的SPI[40]和自适应欠奈奎斯特采样方法[41]。

对于照明光场的调制模式，Hadamard图案的二值特性与DMD的相位调制方式非常契合，因此本文选择Hadamard基用来调制透镜波前。然而，其他调制基也适用，例如随机矩阵[42]、傅里叶(Fourier)基[14]、离散

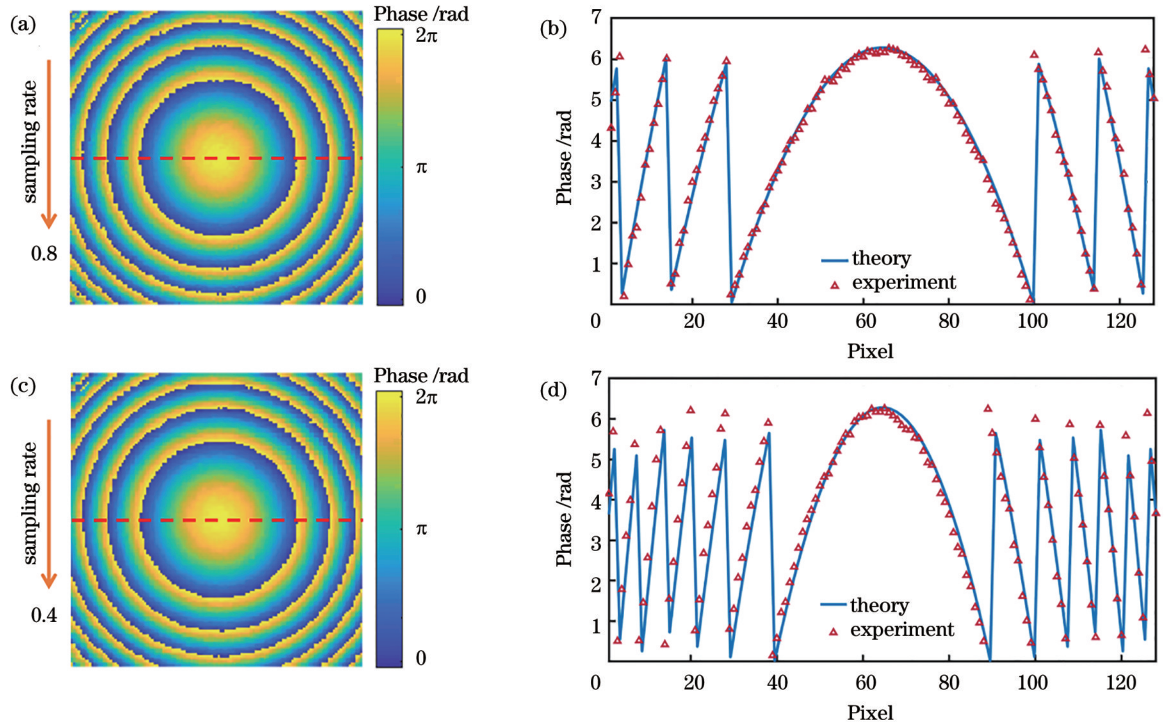

图 6　名义焦距为 1000 mm 的光学透镜在不同采样率下的相位检测结果。(a)、(b)采样率为 0.8 时，重建的截断相位与理论值的对比；(c)、(d)采样率为 0.4 时，重建的截断相位与理论值的对比

Fig. 6　Phase detection results of optical lens with nominal focal length of 1000 mm at different sampling rates. (a), (b) Reconstructed truncated phases compared with theoretical values under sampling rate of 0.8; (c), (d) reconstructed truncated phases compared with theoretical values under sampling rate of 0.4

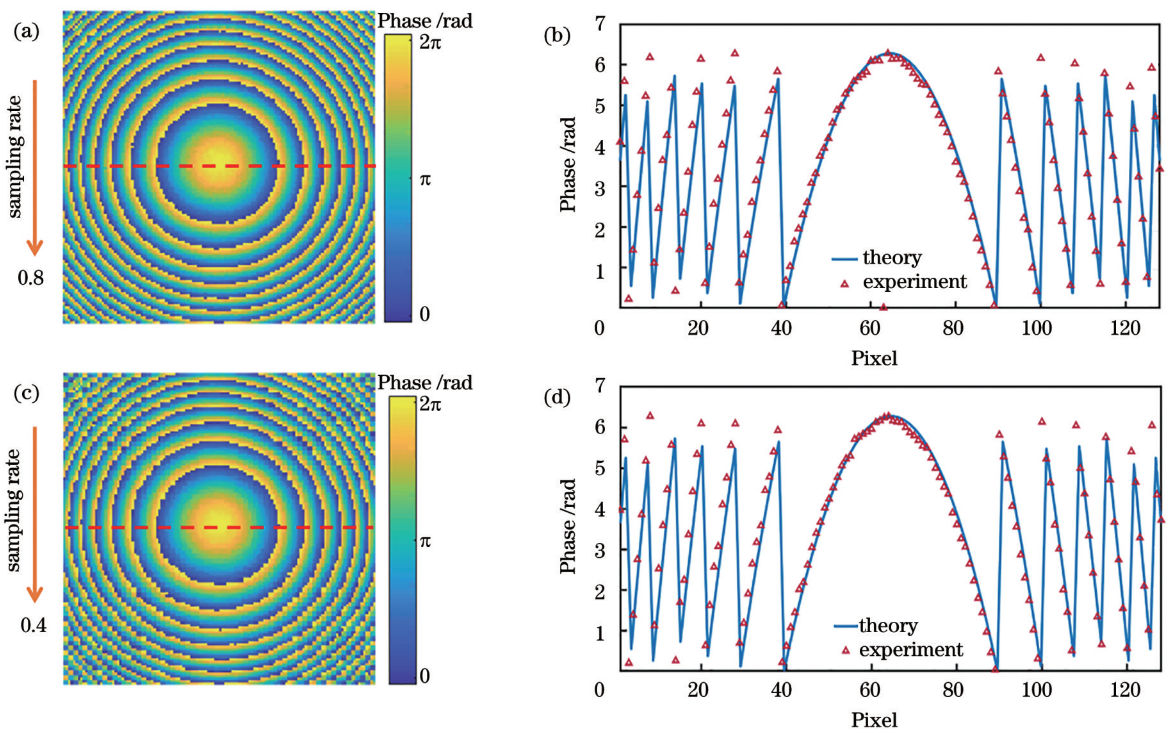

图 7　名义焦距为 500 mm 的光学透镜在不同采样率下的相位检测结果。(a)、(b)采样率为 0.8 时，重建的截断相位与理论值的对比；(c)、(d)采样率为 0.4 时，重建的截断相位与理论值的对比

Fig. 7　Phase detection results of optical lens with nominal focal length of 500 mm at different sampling rates. (a), (b) Reconstructed truncated phases compared with theoretical values under sampling rate of 0.8; (c), (d) reconstructed truncated phases compared with theoretical values under sampling rate of 0.4

余弦变换(DCT)基[38]、轨道角动量(OAM)光束[35-37]等。同时,本文采用二元光栅法在DMD上实现对多步移相的相位调制,其他方法,如Lee方法[43]和超像素方法[44]也同样适用。

4 结 论

综上所述,本文提出并演示了一种基于DMD共路移相干涉单像素波前成像的透镜相位检测方法。实验结果表明,对文中所述的两种具有不同名义焦距的光学透镜,采用四步移相干涉法测量精度更高。同时,本文还研究得出,重建透镜相位图像空间分辨率越高,由此计算得到的透镜焦距精度越高,即相位检测精度越高。为了减少透镜相位成像时间,采用三步移相干涉法结合降采样的策略,对具有不同名义焦距的光学透镜进行相位重建和焦距计算,均能得到精度较高的焦距测量值。本文所提方法为可见光波段的透镜相位检测提供了一种既简单又经济的手段。此外,得益于单像素探测器自身的优势,该方法有望用于深紫外、远红外、太赫兹等特殊波段,以及二维探测器价格昂贵,或少数波段二维探测器尚不成熟甚至还没有的场合。

参 考 文 献

[1] Gao Y, Lim E W, Yang A, et al. The impact of spectacle lenses for myopia control on visual functions[J]. Ophthalmic & Physiological Optics, 2021, 41(6): 1320-1331.

[2] 孔梅梅, 潘世成, 袁东, 等. 方腔结构非球面液体透镜的设计与分析[J]. 激光与光电子学进展, 2023, 60(21): 2122005.
Kong M M, Pan S C, Yuan D, et al. Design and analysis of aspheric liquid lens with square cavity structure[J]. Laser & Optoelectronics Progress, 2023, 60(21): 2122005.

[3] 闫超, 胡思怡, 顾波波. 超透镜在显微成像中的进展:设计、加工及应用[J]. 激光与光电子学进展, 2024, 61(2): 0211028.
Yan C, Hu S Y, Gu B B. Advances in microscopic imaging with metalenses: design, fabrication, and applications[J]. Laser & Optoelectronics Progress, 2024, 61(2): 0211028.

[4] Knauer M C, Kaminski J, Hausler G. Phase measuring deflectometry: a new approach to measure specular free-form surfaces[J]. Proceedings of SPIE, 2004, 5457: 366-376.

[5] 高锦瑞, 李大海, 赖恒, 等. 基于相位测量偏折术的透镜波前像差测量[J]. 激光与光电子学进展, 2022, 59(2): 0212001.
Gao J R, Li D H, Lai H, et al. Measurement of wavefront aberration of lens based on phase measuring deflectometry[J]. Laser & Optoelectronics Progress, 2022, 59(2): 0212001.

[6] 阮一郎, 李大海, 余林治, 等. 基于相位测量偏折术的成像透镜轴外点波像差测量[J]. 中国激光, 2022, 49(21): 2104003.
Ruan Y L, Li D H, Yu L Z, et al. Off-axis point wave aberration testing for imaging lens based on phase measuring deflectometry[J]. Chinese Journal of Lasers, 2022, 49(21): 2104003.

[7] Zhao P, Gao N, Zhang Z H, et al. Performance analysis and evaluation of direct phase measuring deflectometry[J]. Optics and Lasers in Engineering, 2018, 103: 24-33.

[8] Singh P, Faridi M S, Shakher C, et al. Measurement of focal length with phase-shifting Talbot interferometry[J]. Applied Optics, 2005, 44(9): 1572-1576.

[9] Primot J. Theoretical description of Shack-Hartmann wave-front sensor[J]. Optics Communications, 2003, 222(1/2/3/4/5/6): 81-92.

[10] Xu J H, Zhuang S L. Measurement of lens focal length with Hartmann-Shack wavefront sensor based on 4F system[J]. Optik, 2015, 126(13): 1303-1306.

[11] Clemente P, Durán V, Tajahuerce E, et al. Single-pixel digital ghost holography[J]. Physical Review A, 2012, 86(4): 041803.

[12] Katz O, Bromberg Y, Silberberg Y. Compressive ghost imaging[J]. Applied Physics Letters, 2009, 95(13): 131110.

[13] Edgar M P, Gibson G M, Padgett M J. Principles and prospects for single-pixel imaging[J]. Nature Photonics, 2019, 13: 13-20.

[14] Zhang Z B, Wang X Y, Zheng G A, et al. Fast Fourier single-pixel imaging via binary illumination[J]. Scientific Reports, 2017, 7: 12029.

[15] 俞文凯, 唐菲遥, 王硕飞, 等. 动态单像素成像[J]. 激光与光电子学进展, 2021, 58(10): 1011013.
Yu W K, Tang F Y, Wang S F, et al. Dynamic single-pixel imaging[J]. Laser & Optoelectronics Progress, 2021, 58(10): 1011013.

[16] 赵梓栋, 杨照华, 余远金. 单像素成像技术研究进展[J]. 中国激光, 2022, 49(19): 1917001.
Zhao Z D, Yang Z H, Yu Y J. Research progress of single pixel imaging[J]. Chinese Journal of Lasers, 2022, 49(19): 1917001.

[17] 王一同, 周宏强, 闫景道, 等. 基于深度学习算法的计算光学研究进展[J]. 中国激光, 2021, 48(19): 1918004.
Wang Y T, Zhou H Q, Yan J X, et al. Advances in computational optics based on deep learning[J]. Chinese Journal of Lasers, 2021, 48(19): 1918004.

[18] Tajahuerce E, Durán V, Clemente P, et al. Image transmission through dynamic scattering media by single-pixel photodetection[J]. Optics Express, 2014, 22(14): 16945-16955.

[19] Jin S L, Hui W W, Wang Y L, et al. Hyperspectral imaging using the single-pixel Fourier transform technique[J]. Scientific Reports, 2017, 7: 45209.

[20] Qi Y, Heng L Z, Li L, et al. Hadamard transform-based hyperspectral imaging using a single-pixel detector[J]. Optics Express, 2020, 28(11): 16126-16139.

[21] Olbinado M P, Paganin D M, Cheng Y, et al. X-ray phase-contrast ghost imaging using a single-pixel camera[J]. Optica, 2021, 8(12): 1538-1544.

[22] 赵海潇, 郭岩, 李珮明, 等. 单像素成像信噪比分析及其在特殊波段的发展[J]. 激光与光电子学进展, 2021, 58(10): 1011010.
Zhao H X, Guo Y, Li P M, et al. Investigation of single-pixel imaging in signal-to-noise ratio and its development at special wavelength[J]. Laser & Optoelectronics Progress, 2021, 58(10): 1011010.

[23] Shrekenhamer D, Watts C M, Padilla W J. Terahertz single pixel imaging with an optically controlled dynamic spatial light modulator[J]. Optics Express, 2013, 21(10): 12507-12518.

[24] 佘荣斌, 祝永乐, 刘文权, 等. 太赫兹单像素计算成像原理及其应用(特邀)[J]. 红外与激光工程, 2021, 50(12): 20210717.
She R B, Zhu Y L, Liu W Q, et al. Terahertz single-pixel computational imaging: principles and applications (Invited)[J]. Infrared and Laser Engineering, 2021, 50(12): 20210717.

[25] 孙宝清, 江山, 马艳洋, 等. 单像素成像在特殊波段及三维成像的应用发展[J]. 红外与激光工程, 2020, 49(3): 0303016.
Sun B Q, Jiang S, Ma Y Y, et al. Application and development of single pixel imaging in the special wavebands and 3D imaging[J]. Infrared and Laser Engineering, 2020, 49(3): 0303016.

[26] Jiang W J, Yin Y K, Jiao J P, et al. 2, 000, 000 fps 2D and 3D imaging of periodic or reproducible scenes with single-pixel detectors[J]. Photonics Research, 2022, 10(9): 2157-2164.

[27] Sun B, Edgar M P, Bowman R, et al. 3D computational imaging with single-pixel detectors[J]. Science, 2013, 340(6134): 844-847.

[28] Zhao W J, Gao L, Zhai A P, et al. Comparison of common algorithms for single-pixel imaging via compressed sensing[J].

Sensors, 2023, 23(10): 4678.

[29] Clemente P, Durán V, Tajahuerce E, et al. Compressive holography with a single-pixel detector[J]. Optics Letters, 2013, 38(14): 2524-2527.

[30] González H, Martínez-León L, Soldevila F, et al. High sampling rate single-pixel digital holography system employing a DMD and phase-encoded patterns[J]. Optics Express, 2018, 26 (16): 20342-20350.

[31] Martínez-León L, Clemente P, Mori Y, et al. Single-pixel digital holography with phase-encoded illumination[J]. Optics Express, 2017, 25(5): 4975-4984.

[32] Ota K, Hayasaki Y. Complex-amplitude single-pixel imaging[J]. Optics Letters, 2018, 43(15): 3682-3685.

[33] Liu R F, Zhao S P, Zhang P, et al. Complex wavefront reconstruction with single-pixel detector[J]. Applied Physics Letters, 2019, 114(16): 161901.

[34] Zhao W J, Du Z H, Zhai A P, et al. Wavefront imaging of a biological sample using DMD-based single-pixel phase-shifting interferometric techniques: an experimental comparison[J]. Optics Laser Technology, 2024, 172: 110483.

[35] Gao L, Zhao W J, Zhai A P, et al. OAM-basis wavefront single-pixel imaging via compressed sensing[J]. Journal of Lightwave Technology, 2023, 41(7): 2131-2137.

[36] He P, Gao L, Zhao W J, et al. Wavefront single-pixel imaging using a flexible SLM-based common-path interferometer[J]. Optics and Lasers in Engineering, 2023, 168: 107633.

[37] He P, Zhao W J, Zhai A P, et al. Inter-mode interferometry for resolution enhancement of common-path OAM-basis wavefront single-pixel imaging[J]. Optics and Lasers in Engineering, 2024, 175: 107996.

[38] Sun S Z, Zhao W J, Zhai A P, et al. DCT single-pixel detecting for wavefront measurement[J]. Optics & Laser Technology, 2023, 163: 109326.

[39] Du Z H, Zhao W J, Zhai A P, et al. DMD-based single-pixel off-axis interferometry for wavefront reconstruction of a biological sample[J]. Applied Physics Letters, 2023, 123(3): 033702.

[40] 王之润, 何鹏, 赵文静, 等. 软硬件协同实现 DQN-Hadamard 单像素成像的研究[J]. 量子电子学报, 2022, 39(6): 962-972.
Wang Z R, He P, Zhao W J, et al. Research on DQN-Hadamard single-pixel imaging with software and hardware cooperation[J]. Chinese Journal of Quantum Electronics, 2022, 39(6): 962-972.

[41] Xu C W, Zhai A P, Zhao W J, et al. Orthogonal single-pixel imaging using an adaptive under-Nyquist sampling method[J]. Optics Communications, 2021, 500: 127326.

[42] Li X Y, Sun Y F, He Y K, et al. Quantitative imaging for optical field via a single-pixel detector[J]. Signal Processing, 2021, 188: 108173.

[43] Lee W H. Binary computer-generated holograms[J]. Applied Optics, 1979, 18(21): 3661-3669.

[44] Goorden S A, Bertolotti J, Mosk A P. Superpixel-based spatial amplitude and phase modulation using a digital micromirror device[J]. Optics Express, 2014, 22(15): 17999-18009.

Phase-Shifting Common-Path Interferometry for Lens Phase Detection via Single-Pixel Detector

Tao Xingfu[1], Zhai Aiping[1*], Ji Wenjing[1], Zhao Wenjing[1], Wang Dong[1,2**]

[1] *College of Electronic Information and Optical Engineering, Taiyuan University of Technology, Taiyuan* 030024, *Shanxi, China*;

[2] *Key Laboratory of Advanced Transducers and Intelligent Control System, Ministry of Education, Taiyuan University of Technology, Taiyuan* 030024, *Shanxi, China*

Abstract

Objective The traditional 2D detector-based phase measurement methods are always limited by the specific spectral response range, for which single-pixel wavefront imaging provides a new method. A digital micromirror device (DMD)-based single-pixel common-path interference is established, in which Hadamard basis is employed to modulate the target wavefront and the checkerboard partition on the DMD is done to divide the light field into the signal and reference fractions. Meanwhile, phase image formation is implemented as usual with the mathematical principles of single-pixel imaging and phase-shifting algorithms. The results show that with the four-step phase-shifting, the mean relative error of the calculated focal length is as low as 0.0298% when the phase image resolution is 128 pixel×128 pixel for a lens with a nominal focal length of 1000 mm. This method is characterized by a simple device, low cost, and simple calculation principle. Benefiting from the single-pixel detection advantages, this method is expected to be adopted for wavefront detection of lenses or transparent objects in weak light environments, extreme ultraviolet, and far infrared bands. Further, it expands the application scope of single-pixel wavefront imaging.

Methods According to the single-pixel wavefront imaging theory, a DMD-based single-pixel multi-step phase-shifting common-path interferometer is established, in which the Hadamard basis is utilized to modulate the target wavefront, and the checkerboard partition on the DMD is done to divide the light field into the signal and reference fractions and form the interference. Then, the lens wavefront can be reconstructed using the passively detected coefficients correlated with the

Hadamard modulation patterns. Finally, the phase and amplitude of the physical lens can be obtained from the reconstructed complex wavefront. For the wavefront reconstruction, a four/three-step phase-shifting and down-sampling strategy is performed.

Results and Discussions Two lenses with focal lengths of 1000 mm and 500 mm are selected as the targets under test. According to the phase detection results, one can gain the truncation phase distribution and the 3D display of the unwrapped phase. The cross-sections of the measured phases agree well with the theoretical values [Figs. 3(c) and 3(f)]. The measured focal lengths of the lenses are 1000.2 mm and 499.5 mm. The relative errors of the focal lengths between the theoretical values and the measurement ones corresponding to the two lenses are 0.02% and −0.10%, which proves the reconstructed results agree well with the theoretical values and further demonstrates the availability of the phase-shifting common-path interferometry for lens phase detection. Next, the influence of different pinhole sizes on the experimental measurement accuracy is demonstrated, as shown in Table 1. Considering the realistic factors, the 20 μm pinhole is finally selected for subsequent experiments.

Then, as a proof-of-concept under low-resolution circumstances, the phase image of the 1000 mm lens with 64 pixel× 64 pixel is retrieved by employing the four-step phase-shifting method (Fig. 4). The 1000 mm lens is measured five times continuously at two different resolutions. At the resolution of 128 pixel×128 pixel, the measured focal length results are given in Table 2. According to Table 2, the average focal length is 1000.080 mm, and the mean relative error between the measured value and the nominal value of the focal length is 0.0298%. At the resolution of 64 pixel×64 pixel, the measurement results are shown in Table 3, and the average value of the measured focal length and the mean relative error are 999.422 mm and 0.1603% respectively.

Finally, the experiment of improving the measurement speed is carried out. Under the three-step phase-shifting method, the cross-sections of the measured phases are still consistent with the theoretical values (Fig. 5). The measurement results of the above two lenses are 1000.6 mm and 501.6 mm. Compared to the theoretical values, the relative errors are 0.06% and 0.32%. The lens phase is reconstructed by combining the three-step phase-shifting with the down-sampling strategy. For the 1000 mm optical lens (Fig. 6), the measured focal lengths are 1001.4 mm and 1001.9 mm corresponding to sampling rates of 0.8 and 0.4, leading to relative errors of 0.14% and 0.19%, respectively. Regarding the 500 mm optical lens (Fig. 7), the calculated focal lengths are 503.1 mm and 503.4 mm when the sampling rates are set as 0.8 and 0.4, bringing about relative errors of 0.62% and 0.68%, respectively.

Conclusions As far as we know, DMD-based common-path interference single-pixel imaging is first successfully employed to detect cemented doublet with different focal lengths. Experimental results show that whether it is 1000 mm or 500 mm optical lens, the measured focal lengths are much closer to the theoretical ones by adopting the four-step phase-shifting algorithm. The influence of image resolution on the measurement results is investigated, which helps conclude that the mean relative error is as low as 0.0298% when the 128 pixel×128 pixel phase image measured by a four-step phase-shifting algorithm is chosen to calculate the focal length. Additionally, by exploiting the down-sampling strategy, the imaging time is shortened further when the three-step phase-shifting algorithm is adopted for phase retrieval. Thus, we currently provide a simple and cost-effective way for lens detection and further advance the single-pixel imaging technology toward practical applications.

Key words single-pixel wavefront imaging; lens phase detection; phase-shifting interference; common-path interference